



CHORUS

This is the accepted manuscript made available via CHORUS. The article has been published as:

Quasistatic fluid-fluid displacement in porous media: Invasion-percolation through a wetting transition

Bauyrzhan K. Primkulov, Stephen Talman, Keivan Khaleghi, Alireza Rangriz Shokri, Rick Chalaturnyk, Benzhong Zhao, Christopher W. MacMinn, and Ruben Juanes

Phys. Rev. Fluids **3**, 104001 — Published 11 October 2018

DOI: [10.1103/PhysRevFluids.3.104001](https://doi.org/10.1103/PhysRevFluids.3.104001)

Quasi-Static Fluid-Fluid Displacement in Porous Media: Invasion-Percolation Through a Wetting Transition

Bauyrzhan K. Primkulov,¹ Stephen Talman,² Keivan Khaleghi,² Alireza Rangriz Shokri,²
Rick Chalaturnyk,² Benzhong Zhao,³ Christopher W. MacMinn,⁴ and Ruben Juanes^{1,*}

¹*Department of Civil and Environmental Engineering,
Massachusetts Institute of Technology, Cambridge, MA, USA*

²*Department of Civil and Environmental Engineering,
University of Alberta, Edmonton, Canada*

³*Department of Civil Engineering, McMaster University, Hamilton, ON, Canada*

⁴*Department of Engineering Science,
University of Oxford, Oxford, United Kingdom*

(Dated: September 21, 2018)

Abstract

We study the influence of wettability on the morphology of fluid-fluid displacement through analog porous media in the limit of vanishing flow rates. We introduce an invasion-percolation model that considers cooperative pore filling and corner flow mechanisms, and captures interface motion at the pore-scale for all quasi-static flow regimes between strong drainage and strong imbibition. We validate the method against recent experimental observations of wetting transition in microfluidic cells patterned with circular posts, and we use it to explore the sensitivity of fluid invasion to wettability heterogeneity, post spacing, and post height. Our model therefore extends the Cieplak-Robbins description of quasi-static fluid invasion by reproducing the wetting transition in strong imbibition, a feature that requires incorporating three-dimensional effects.

* juanes@mit.edu

23 I. INTRODUCTION

24 Fluid-fluid displacement in porous media is a rich phenomenon, where the interplay be-
25 tween wettability, pore-scale disorder, viscosity ratio of invading and defending fluids, and
26 magnitude of viscous forces relative to that of capillary forces (defined by the capillary num-
27 ber, Ca) generates a wide spectrum of interface patterns. The study of the mechanisms
28 behind these patterns is of relevance to many practical applications. For instance, in the
29 limit of high capillary numbers, the displacement of high-viscosity fluid by a low-viscosity
30 fluid develops a morphology akin to diffusion-limited aggregation [1–3], and hence serves
31 as an analog system to dielectric breakdown [4], electrodeposition [5], and propagation of
32 forest fires [6]. Furthermore, both high and low capillary number displacement regimes have
33 direct practical significance in soil remediation and chemical filters [7], fuel cell technology
34 [8], carbon sequestration [9], oil recovery [10], and design of microfluidic devices [11].

35 For a given fluid pair, the wettability of the porous medium plays a fundamental role in
36 defining the nature of the displacement both at pore [12–14] and macroscopic scales [15, 16].
37 Wettability is often defined through the contact angle θ between the fluid-fluid interface
38 and the solid. We adopt the convention that θ is measured from the invading phase, such
39 that $\theta > 90^\circ$ corresponds to drainage, and $\theta < 90^\circ$ corresponds to imbibition. In the limit
40 of low capillary number and strong drainage (i.e. strongly non-wetting invading fluid), the
41 fluid-fluid interface advances through capillary fingering and forms a jagged interface that
42 tends to trap defending fluid throughout the displacement [17–20]. In weak imbibition (i.e.
43 weakly wetting invading fluid), in contrast, the interface tends to move as a compact front
44 [15, 16, 21, 22], where capillary forces work to flatten the interface through cooperative
45 pore filling [23, 24]. While the mechanisms of fluid-fluid displacement in drainage are fairly
46 well explored, fluid-fluid displacement in imbibition continues to challenge our mathematical
47 descriptions.

48 Patterned microfluidic devices offer a convenient way to visualize the fluid-fluid displace-
49 ment in a controlled and repeatable environment. As a quasi-two-dimensional analog of
50 natural porous media, these microfluidic devices are typically fabricated by generating a
51 pattern of posts on a solid surface and confining it between two flat plates, allowing careful
52 control of both pore geometry and wettability. Early microfluidic experiments [1, 17–19]
53 explored the interplay between viscous and capillary forces in drainage and weak imbibition,

54 and their findings are in line with the theory [15, 16, 25, 26]. Only recently has this body of
55 work been extended to strong imbibition, where new displacement patterns emerge [27, 28].

56 Zhao *et al.* [27] conducted a series of viscously unstable experiments on microfluidic
57 devices with an irregular pattern of circular posts, where water displaced oil radially from
58 the center of the flow cell at different injection rates and different contact angles between 150°
59 (strong drainage) and 7° (strong imbibition). The authors reported a new wetting transition
60 in the strong imbibition regime ($7^\circ < \theta < 45^\circ$): flow reverts from compact displacement to
61 a corner-flow regime, where the invading fluid advances by preferentially coating the corners
62 between the posts and top/bottom plates of the flow cell. Similar observations were recently
63 reported on a regularly patterned microfluidic cell with square posts [28]. These new findings
64 may have significant implications for physical modeling of the displacement processes with
65 tunable wetting conditions.

66 Several computational approaches are available to model pore-scale fluid-fluid displace-
67 ment. These include, in decreasing order of fidelity (and required computational power):
68 [29] (1) molecular dynamic simulations; (2) numerical solutions of the Navier-Stokes equa-
69 tions with interface and contact-line tracking; (3) lattice or dissipative particle dynamics
70 based models; and (4) pore-network models. The first three approaches require a detailed
71 description of the pore geometry, and are not yet practical for obtaining macroscopic inva-
72 sion patterns. Pore-network models, on the other hand, rely on a simplified pore geometry
73 and a simplified description of the flow, and are therefore less computationally demanding
74 [30]. The geometric details as well as simplifying assumptions of the interface vary widely
75 from one study to another [31–34].

76 Two particular subclasses of pore-network models are of interest in reproducing the ex-
77 perimental observations of Zhao *et al.* [27] in the limit of very low Ca: invasion-percolation
78 algorithms [19, 20] and the quasi-static interface tracking method of Cieplak and Robbins
79 [23, 24]. Invasion-percolation algorithms are robust, but can only capture the invading in-
80 terface morphology in strong drainage. The interface-tracking algorithm of Cieplak and
81 Robbins [23, 24] is applicable to wettabilities from strong drainage to weak imbibition,
82 although it is susceptible to the biases of user-defined conventions in injection pressure in-
83 crements and scanning order of pore invasion mechanisms. Neither method extends to the
84 corner-flow regime of strong imbibition.

85 Here, we implement an invasion-percolation algorithm that qualitatively reproduces fluid-

86 fluid displacement morphologies for all wettabilities, from strong drainage to strong imbi-
87 bition. By building on the work of Cieplak and Robbins [23, 24], we are able to explicitly
88 calculate the critical pressures of pore-scale instabilities, including the instability events po-
89 tentially responsible for the corner flow regime in strong imbibition [27]. This new approach
90 eliminates the need for user-assigned pressure increments, instead advancing the interface
91 in the manner of invasion-percolation. Our quasi-static algorithm captures the fluid-fluid
92 displacement in the limit of very low Ca , where viscous forces can be neglected.

93 The algorithm was implemented on a two-dimensional flow geometry similar to the one in
94 the experiments of Zhao *et al.* [27]. We used the model to capture the wetting transition in
95 strong imbibition and explored the sensitivity of the flow pattern to pore-scale heterogeneity
96 in contact angle, post spacing, and to three-dimensional effects of finite post height.

97 II. METHOD

98 Experimental observations of fluid-fluid displacement in different wettability regimes pro-
99 vide an intuitive way to understand the underlying assumptions behind different models of
100 multiphase flow.

101 In drainage, the invasion pattern advances by overcoming local capillary entry pressures
102 within the porous medium [18]. In the limit of vanishing Ca , viscous dissipation can be
103 neglected and the invasion process is well captured by the invasion-percolation algorithm
104 [20, 35, 36]. This approach replaces the pore space with a network of nodes (pores) and
105 edges (throats). Throats that contain a fluid-fluid interface are considered active. Every
106 active throat is ranked according to its critical capillary pressure, which can be calculated
107 from the throat size. The invading fluid moves by advancing locally into the throat with the
108 lowest critical capillary pressure, resulting in invasion avalanches and displacement fronts
109 that often loop on themselves and trap clusters of the defending fluid behind the advancing
110 front.

111 While the invasion-percolation algorithm is in good agreement with experiments in
112 drainage [18], it fails to reproduce the invading fluid pattern during imbibition. Here, coop-
113 erative pore filling mechanisms make the invading pattern smoother, and invasion proceeds
114 through compact fronts [19].

115 Cieplak and Robbins [23, 24] showed that in order to capture cooperative pore filling

116 effects during imbibition one needs to account for the local pore geometry [23, 24]. They
117 approximated the porous medium by placing posts on a regular 2D lattice; every post was
118 assigned a random radius from a uniform distribution. The interface consisted of a collection
119 of arcs between the posts. Every arc intersected nearby posts at a prescribed contact angle
120 and curvature defined by the Laplace pressure Δp .

121 Cieplak and Robbins [23, 24] introduced three types of instabilities: “burst” (no stable
122 arc at given Δp), “touch” (interface touches opposite post), and “overlap” (two neighbour-
123 ing interfaces coalesce within the pore). The algorithm moves the fluid-fluid interface at
124 fixed injection pressures by searching for unstable arcs and replacing them with new stable
125 configurations (pore invasion). When no unstable arcs are found, the invading fluid pressure
126 is increased to induce further advance.

127 Unlike the invasion-percolation algorithm, local interface instabilities are sensitive to
128 geometric configurations of neighbouring arcs, allowing for cooperative pore filling (mostly
129 dominated by touch and overlap instabilities) during imbibition. Moreover, the algorithm
130 produces results nearly identical to invasion-percolation algorithm in drainage, where burst
131 instabilities are prevalent[24]. Thus, the model of Cieplak and Robbins [23, 24] extends the
132 description of quasi-static fluid-fluid displacement in porous media from strong drainage to
133 weak imbibition.

134 At the same time, Cieplak and Robbins [23, 24] acknowledged that the arbitrary se-
135 quence of pressure increments affects the morphology of simulated invasion fronts. Unlike
136 the invasion-percolation algorithm, where the sequence of local interface advances is de-
137 termined through global critical pressure ranking, the Cieplak and Robbins [23, 24] model
138 advances unstable arcs in the order they are discovered by a user-defined search convention.
139 Moreover, the choice of pressure increments often results in more than one type of insta-
140 bility within the same arc; instabilities are removed by authors’ convention where touch
141 instabilities are removed first and burst instabilities are removed last.

142 We found that by reformulating the original approach of Cieplak and Robbins [23, 24], one
143 can explicitly calculate critical pressures of all instability events and advance the interface
144 in an invasion-percolation-like manner. The interface moves based on the ranking of critical
145 pressures that are calculated from local arc and post geometries. Thus, this new formulation
146 eliminates the need for arbitrary pressure increments and allows the least stable arcs to
147 advance first. Below we describe the details of the new formulation followed by the algorithm

148 in the spirit of invasion-percolation.

149 Consider a set of neighboring posts (FIG. 1). On every image, posts are numbered from
 150 1 to 3 (where applicable): left post is 1, right post is 2, and the top post is 3 (FIG. 1(b)-
 151 (d)). Each post is defined through its radius, location expressed in Cartesian coordinates,
 152 and a contact angle. For example post 1 has radius r_1 , location (x_1, y_1) , and contact angle
 153 θ_1 measured from the invading fluid between posts 1 and 2 (FIG. 1(a)). Without loss of
 154 generality, we rotate and translate the coordinate system so that points (x_1, y_1) , (x_2, y_2) ,
 155 (x_3, y_3) turn into $(0, 0)$, $(X_2, 0)$, (X_3, Y_3) .

156 For the description that follows, we assume that the posts are tall enough that the events
 157 considered in FIG. 1(b)-(d) can be formulated in a two-dimensional sense. The validity and
 158 limitations of this assumption are further explored in section III.

159 Consider an interface of radius of curvature r_p that meets post 1 at contact angle θ_1 (FIG.
 160 1(a)). We define d_1 to be the distance from the center of interface curvature to the center of
 161 post 1. Given an expression for value of $\angle ACP$, the distance d_1 can be determined from the
 162 law of cosines for $\triangle ACP$. Both $\angle PCU$ and $\angle TCA$ are equal to $\pi/2$ and $\angle UCT$ is $\pi - \theta_1$.
 163 Since $\angle ACP + \angle PCU + \angle UCT + \angle TCA = 2\pi$, then $\angle ACP = \theta_1$. Therefore,

$$164 \quad d_1(r_p, \theta_1) = AP = \sqrt{r_1^2 + r_p^2 - 2r_1r_p \cos \theta_1}. \quad (1)$$

165 Equation (1) defines the distance between the center of curvature (X_p, Y_p) and the center
 166 of post 1 $(0, 0)$. This means that point (X_p, Y_p) lies on a circle concentric with post 1 and
 167 radius d_1 , where the interface satisfies the contact angle θ_1 and has radius of curvature r_p .
 168 All points satisfying this requirement are shown as a dashed line on FIG. 1(a).

169 A similar construction for an interface intersecting with a second post of radius r_2 and a
 170 contact angle θ_2 centered at $(X_2, 0)$ defines a second circle centered at post 2. For a given
 171 r_p , this second circle (dashed line FIG. 1(a) opening to the right) will share either two, one
 172 or zero common points with the set of potential centers of curvature for the interfaces which
 173 stably contact post 1. FIG. 1(a) shows a case where the interface is stable. Considering only
 174 the case when the invading fluid is sourced from below the X -axis, the stable interface touch-
 175 ing both posts will be centered at a point (X_p, Y_p) which is determined to simultaneously
 176 satisfy

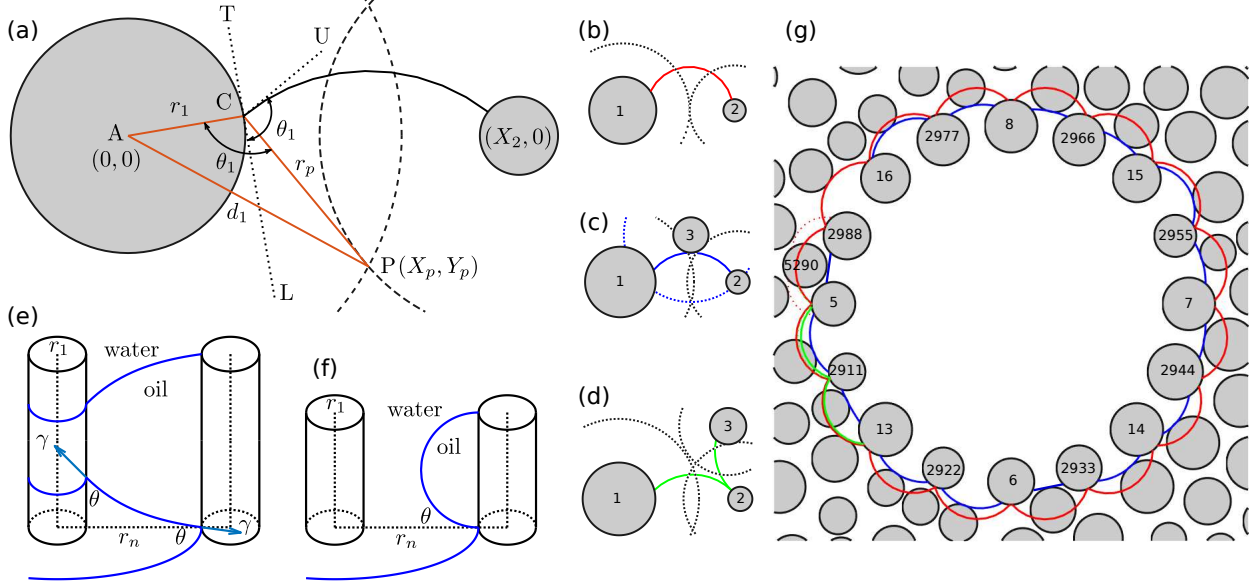


FIG. 1. (a) Invasion front configuration between two posts; (b) Burst event: unstable interface (red line) advances into the pore; (c) Touch event: interface touches the nearest post; (d) Overlap event: two fronts (green lines) coalesce on post surface and fill the pore; (e) Corner flow event: corner meniscus touches and coats the neighbouring post; (f) Capillary bridge event: corner menisci coalesce mid-post before reaching the next post; (g) Invading front configuration with post IDs: red, blue, green interfaces correspond to “burst”, “touch”, “overlap” critical interfaces.

$$177 \quad X_p^2 + Y_p^2 = d_1(r_p, \theta_1)^2, \quad (2a)$$

$$178 \quad (X_p - X_2)^2 + Y_p^2 = d_2(r_p, \theta_2)^2, \quad (2b)$$

$$179 \quad Y_p \leq 0. \quad (2c)$$

180 Subtraction of (2a) and (2b), allows for the direct calculation of X_p and then Y_p can be
 181 trivially found as the negative root of equation (2a). Equation (2c) ensures that one selects
 182 the correct root when solving for Y_p (FIG. 1(a)).

183 The equations considered here are simplified significantly by the choice of post placement.
 184 For posts located at generic grid points, the post centers can be simply translated and
 185 subsequently rotated to achieve this configuration. Following calculations in this modified
 186 coordinate system the results can be simply rotated and translated back to the original
 187 coordinate system.

188 We are now ready to define several instability events that determine interface propaga-
 189 tion. Following the work of Cieplak and Robbins [23, 24], we consider “burst”, “touch”,
 190 and “overlap” events, and we additionally introduce a new class of “corner” events. The
 191 order and frequency of these pore-level events ultimately define the shape of the quasi-static
 192 invasion pattern. Below we find the critical Laplace pressures Δp (corresponding to radius
 193 of curvature r_p via the Young-Laplace equation, $1/r_p = \Delta p/\gamma$) at which each event takes
 194 place.

195 **Burst Event**

196 As the pressure of the invading phase increases, the radius of interface curvature r_p
 197 decreases. This results in lower values for both d_1 and d_2 . As a result, increasing Δp reduces
 198 the radii of the dashed lines in FIG. 1(a), and the number of their intersection points
 199 (solutions for Equation (2)) changes from 2 to 1, and eventually 0. This means that there is
 200 no longer a stable interface between posts 1 and 2; this event is referred to as “burst” (see
 201 FIG. 1(b)). The “burst” event coincides with the last stable configuration of the interface
 202 between two posts at given contact angles θ_1 and θ_2 . This occurs when there is only a
 203 single root to Equation (2), and also corresponds to the case when $Y_p = 0$ (which implies
 204 a zero discriminant in the quadratic equation). Introducing this condition in Equation (2)
 205 allows finding the critical radius of curvature r_p that corresponds to “burst” as a tangential
 206 intersection of dashed circles in FIG. 1(a):

$$207 \quad X_p^2 = d_1(r_p, \theta_1)^2, \quad (3a)$$

$$208 \quad (X_p - X_2)^2 = d_2(r_p, \theta_2)^2. \quad (3b)$$

209 Equations (3) can be rearranged to give a quadratic equation in r_p ; with the burst radius
 210 chosen to yield a positive burst pressure.

211 **Touch Event**

212 The “touch” event refers to the configuration depicted in FIG. 1(c). Here, the interface
 213 tangentially intersects the third post centered at (X_3, Y_3) and with radius r_3 . This configu-

214 ration can be viewed as the intersection of black dotted lines and the circle of radius $r_p + r_3$
 215 centered at (X_3, Y_3) , represented by the blue dotted line in FIG. 1(c):

$$216 \quad X_p^2 + Y_p^2 = d_1(r_p, \theta_1)^2, \quad (4a)$$

$$217 \quad (X_p - X_2)^2 + Y_p^2 = d_2(r_p, \theta_2)^2, \quad (4b)$$

$$218 \quad (X_p - X_3)^2 + (Y_p - Y_3)^2 = (r_p + r_3)^2. \quad (4c)$$

219 Equation (4) can be solved analytically for the critical value of r_p that satisfies the “touch”
 220 condition. Again, the touch condition given by the solution of Equation (4) can be reduced
 221 to a quadratic equation in r_p , although the expansion to this form involves some laborious
 222 algebra.

223 **Overlap Event**

224 Cieplak and Robbins [23, 24] defined the “overlap” event as an instability where two
 225 advancing contact lines meet on the surface of a post (see FIG. 1(d)). The solution to the
 226 overlap radius of curvature can be written as the intersection of three circles—the interface
 227 between posts 1 and 2, the interface between posts 2 and 3, and the circle corresponding to
 228 the surface of post 2:

$$229 \quad (X - X_{p12})^2 + (Y - Y_{p12})^2 = r_p^2, \quad (5a)$$

$$230 \quad (X - X_{p23})^2 + (Y - Y_{p23})^2 = r_p^2, \quad (5b)$$

$$231 \quad (X - X_2)^2 + Y^2 = r_2^2. \quad (5c)$$

232 Here (X_{p12}, Y_{p12}) and (X_{p23}, Y_{p23}) , which are also functions of r_p , denote the centers of
 233 curvature for interfaces between posts 1 and 2, and 2 and 3, respectively. Equation (5)
 234 coupled with solutions for (X_{p12}, Y_{p12}) and (X_{p23}, Y_{p23}) can be solved numerically for a critical
 235 value of r_p .

236 The underlying assumption in the above equations is that both interfaces in FIG. 1(d)
 237 have the same radius of curvature r_p . In a quasi-static process, as assumed here, the pressure
 238 is spatially uniform in both invading and defending fluids with a Laplace pressure drop

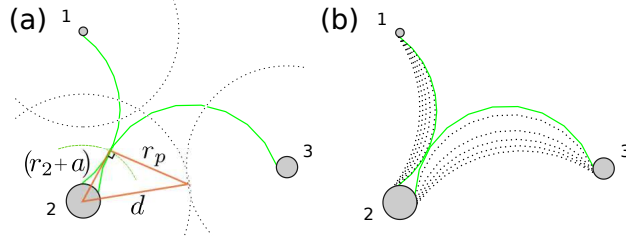


FIG. 2. (a) Schematic diagram of menisci coalescence away from the post surface. (b) The diagram demonstrates *drainage overlap* at $\theta > 90^\circ$: menisci coalesce inside the pore space, leaving trapped oil on the wall of the invaded post.

239 between them. Thus, we can assume that $\Delta p_{12} = \Delta p_{23}$ in overlap event calculations.
 240 Therefore, from the Young-Laplace equation, we have that $\frac{\gamma}{r_{p12}} = \frac{\gamma}{r_{p23}}$ or $r_{p12} = r_{p23} = r_p$.

241 Drainage Overlap Event

242 The original definition of “overlap” event by Cieplak and Robbins [24] is valid only for
 243 $\theta \leq 90^\circ$. When $\theta > 90^\circ$, the two menisci coalesce away from the post, trapping some
 244 defending liquid on the post wall [11], as illustrated for $\theta = 120^\circ$ in FIG. 2(b). This effect
 245 has been largely ignored in pore-level simulations, and a careful experimental investigation
 246 was only reported recently by Lee *et al.* [11].

247 Consider the “drainage overlap” configuration in FIG. 2(a), where overlap occurs at
 248 $\theta > 90^\circ$ and a distance a away from post 2. The solution for this coalescence can be
 249 obtained as an intersection of the two menisci and a circle of radius $(r_2 + a)$ concentric with
 250 post 2:

$$251 \quad (X - X_{p12})^2 + (Y - Y_{p12})^2 = r_p^2, \quad (6a)$$

$$252 \quad (X - X_{p23})^2 + (Y - Y_{p23})^2 = r_p^2, \quad (6b)$$

$$253 \quad (X - X_2)^2 + Y^2 = (r_2 + a)^2. \quad (6c)$$

254 Noting that $(r_2 + a)^2 = d^2 - r_p^2$, where d^2 is analogous to equation (1), unknown a can be
 255 eliminated from the above expressions. This allows solving “drainage overlap” numerically
 256 for the critical value of r_p .

257 **Corner and Capillary Bridge Events**

258 In addition to the events described above, all of which apart from “overlap” for $\theta > 90^\circ$
259 had already been identified previously [23, 24], Zhao *et al.* [27] experimentally observed
260 a transition from pore invasion in weak imbibition to *corner flow* in strong imbibition.
261 In order to capture this transition it is necessary to consider the shape of the fluid-fluid
262 interface in 3D. When the solid walls have high affinity for the invading liquid, the liquid
263 accumulates in corners between the posts and the top/bottom plates of the cell, adopting a
264 constant-curvature configuration shown in FIG. 1(e).

265 In our model, a “corner” event occurs when the interface swells sufficiently to touch a
266 neighboring post; this allows flow towards the corner of the neighbor post. The distance
267 from the center of the wetted post to the surface of its nearest neighbor is denoted by r_n .
268 This distance can be estimated from a force balance on the corner liquid in the vertical
269 direction [37]:

$$270 \quad 2r_1 \cos \theta_1 - 2r_n \sin \theta_1 + (r_n^2 - r_1^2)\Delta p/\gamma = 0. \quad (7)$$

271 Equation (7) can be used to determine the critical pressure differential across the interface
272 that is required for a “corner” event for every post on the invasion front. This equation is
273 valid when the height of the posts is significantly taller than the spacing between the posts.

274 When the post height is comparable to the post spacing, the top and bottom corner
275 menisci might intersect in the middle of the post before a corner event. This results in
276 the coalescence of the two interfaces, and invading liquid coats the post in the shape of a
277 *capillary bridge* (FIG. 1(f)). In this case, we use the constant interface curvature equation
278 shown in Appendix A to find the pressure at which mid-post coalescence takes place. A
279 more detailed discussion of the corner liquid interface shape and validity of Equation (7) is
280 given in Appendix A.

281 **Invasion Algorithm**

282 The closest analog to the invasion algorithm presented here is the invasion-percolation
283 method [20, 35, 36], where the invasion front advances by overcoming threshold pressures
284 associated with pore throats. At every step, a pore with the lowest threshold pressure gets

285 invaded first; the interface is updated and the algorithm proceeds to the next invasion step.
286 The simplicity of invasion-percolation leaves very little room for misinterpretation, but it
287 has traditionally been applied only in strong drainage.

288 The quasi-static invasion of the fluid-fluid interface is governed entirely by the critical
289 pressures of “burst”, “touch”, “overlap”, and “corner” events. To illustrate how the pore-
290 level threshold pressures combine to determine the evolution of the invasion front, consider
291 the initial configuration in FIG. 1(g). This initial invasion front is obtained by connecting
292 the innermost posts, a procedure which does not necessarily produce a stable front. Here,
293 every post has an identification number.

294 We calculate the critical invasion pressures for pore-scale events by solving Equations
295 (3)–(7) for every post on the invasion front. To advance the invading fluid, we traverse the
296 invasion front and select the post with the smallest critical invasion pressure Δp (e.g., a
297 “touch” instability for the interface at post 5 in FIG. 1(g)).

298 The manner in which the invasion front changes following an event depends on the type
299 of instability that takes place. If a “burst” or “touch” instability occurs, the nearest post to
300 the interface is added to invasion front (FIG. 1(b)-(c)). If the least stable event is “overlap”,
301 the post where the contact lines meet is removed from the invasion front.

302 Finally, if a “corner” flow event occurs, a newly captured post is added to the list of
303 *corner invasion* posts. We keep track of this list separately from all other events because
304 the manner in which corner menisci advance is distinctly different. As we show later, this
305 leads to competition between corner invasion and cooperative pore filling invasion at some
306 contact angles, leading to the transition in pore-level displacement mechanism observed by
307 Zhao *et al.* [27]. We assume that cooperative pore filling front posts are also coated in their
308 corners, so the corner list is at least as long as the other list; an assumption that is reasonable
309 for the quasi-static description we employ here, but which will likely be inaccurate at very
310 high capillary numbers, when viscous forces dominate and films of the defending fluid are
311 left behind.

312 By following these simple rules, one can capture the complexity of invasion patterns and
313 their relation to substrate wettability. Although this method was built with the framework
314 initially proposed by Cieplak and Robbins [24] in mind, there are several features of our
315 approach that are important to note.

316 Firstly, the evolution of the interface in the algorithm of Cieplak and Robbins [24] was

317 somewhat sensitive to the arbitrary selection of pressure increments and the order in which
318 the invasion mechanisms were scanned. In the Cieplak and Robbins [24] study, after each
319 pressure increment, every interface was scanned for “burst”, “touch”, and “overlap” in
320 sequence, and an unstable interface was allowed a single step forward. This means that
321 the natural order of the instability events could be disturbed with a poor choice of pressure
322 increments or scanning order; a shortcoming acknowledged by the authors [23, 24]. In
323 contrast, our algorithm always advances the *least stable* interface within the invasion front,
324 therefore eliminating arbitrariness.

325 Secondly, by maintaining the list of critical pressures, new computations only need to
326 be performed in the neighborhood of newly invaded pores. This feature may prove to be
327 especially useful should the algorithm be extended to a dynamic invasion front (i.e. when
328 taking into consideration the pressure changes associated with viscous forces during the
329 motion of the invasion front as in Holtzman and Segre [31]).

330 Finally, within the current framework, we can easily assign unique contact angles to
331 individual posts. We utilize this feature to generate different realizations of the same invasion
332 experiment. That is, for every realization, we assign a random contact angle for every
333 post from a narrow distribution centered around a global mean. This brings us closer to
334 experimental conditions, where small local deviations from the average contact angle of the
335 substrate exist due to material impurities and inhomogeneity from the fabrication process.

336 III. RESULTS AND DISCUSSION

337 We use the model described in the previous section to address the following objectives:
338 (1) we test whether our method is able to fully capture the invasion-pattern morphology
339 through the wetting transition from strong drainage to strong imbibition; (2) we explore the
340 sensitivity of the wetting transition to local perturbations in contact angles through pore-
341 level event statistics and the macroscopic fractal dimension; (3) we study the links between
342 pore spacing and mechanisms of pore-level displacement; (4) finally, we explore the limits of
343 our model by introducing three-dimensional effects with finite post heights within the flow
344 geometry.

345 The baseline pore geometry used in this work was generated in a similar manner to Zhao
346 *et al.* [27]. MATLAB’s `pdemesh` was used to generate a circular Hele-Shaw cell configuration

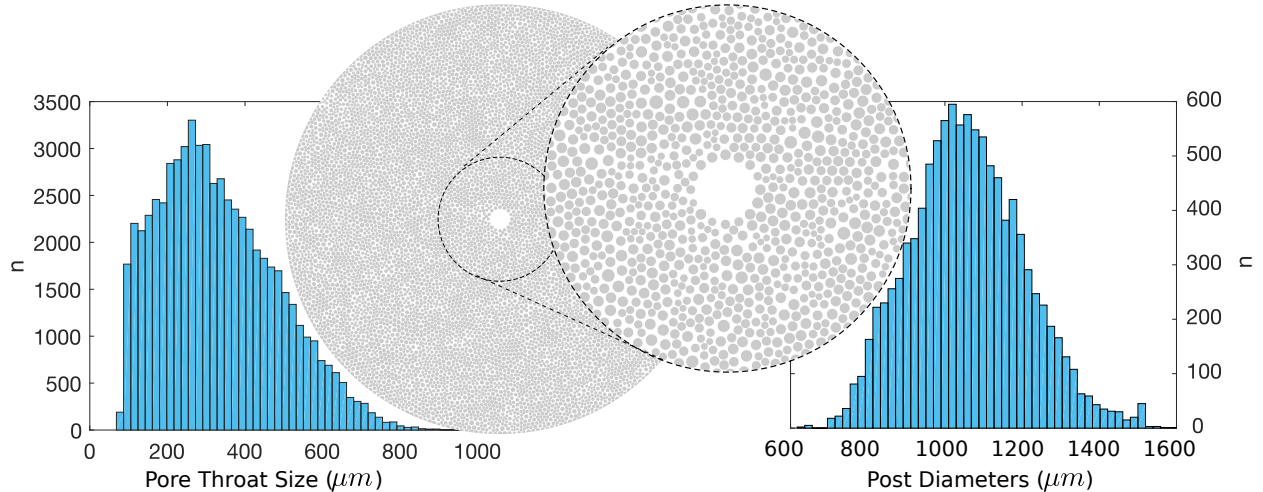


FIG. 3. Generated pore geometry along with post diameter and pore throat size histograms. Posts were placed on irregular triangular lattice generated with MATLAB’s `pdemesh`, and post radii were assigned to 45% of the smallest connected edge.

347 with diameter of 15cm. Centers of the posts were placed at the nodes of the generated
 348 irregular mesh. Then the radius of each individual post was assigned to 45% of the smallest
 349 edge at a corresponding node. The final geometry of posts and the histograms of the resulting
 350 post radii and throat sizes are shown in FIG. 3.

351 **Invasion Front Morphology Through the Wetting Transition**

352 We simulated radial invasion of water into the oil-filled microfluidic cell described above,
 353 with substrate contact angles between 160° (strong drainage) and 10° (strong imbibition).
 354 Pore invasion simulations in FIG. 4 demonstrate that the morphology of the invasion pattern
 355 depends strongly on the wettability of the substrate. In particular, the invasion pattern
 356 becomes more compact as the scenario changes from strong drainage ($\theta = 160^\circ$) to weak
 357 imbibition ($\theta = 45^\circ$), and this is accompanied with a reduction in the amount of trapped
 358 oil behind the invasion front. In strong imbibition, the invading fluid starts to preferentially
 359 accumulate in the corners formed by the posts with the top and bottom plates. This results
 360 in an invasion mechanism that competes with “burst”, “touch”, and “overlap” events.

361 Consider a single post with invading liquid accumulating in its corners with top/bottom
 362 plates. As the pressure of the invading fluid increases, the size of the “corner” meniscus

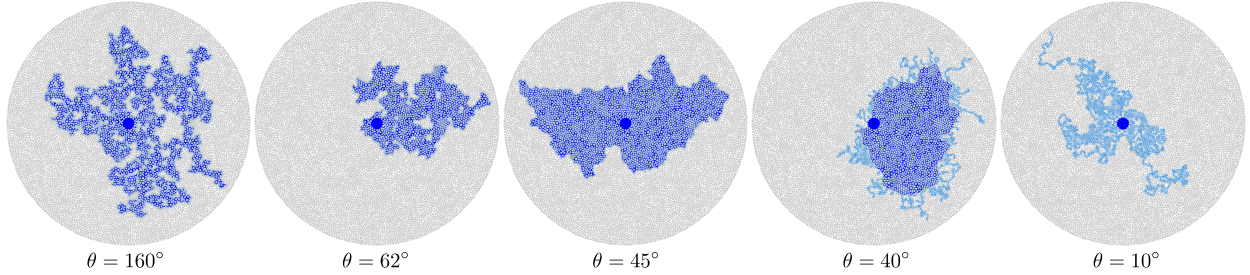


FIG. 4. Immiscible fluid invasion simulation results: algorithm presented in section II covers the full range of pore wettabilities, from strong drainage ($\theta = 160^\circ$) to strong imbibition ($\theta = 10^\circ$). Dark blue regions represent fully invaded pores; light blue regions represent partially invaded pores with coated post corners. We include video files of the invasion process at different wettabilities in supplementary materials.

363 increases, and at some critical pressure the liquid extends far enough to reach the post's
 364 closest neighbour. At this point, the invading liquid flows into the corner of the next post.
 365 Here, invasion proceeds akin to invasion-percolation, albeit on a dual network, where the
 366 sites are the posts and the links are the edges of the corresponding Delaunay tessellation.
 367 This mode of invasion leads to fingering patterns, in contrast with the compact invasion
 368 characteristic of weak imbibition. The pattern at $\theta = 40^\circ$ in FIG. 4 is particularly noteworthy:
 369 here, frequencies of *cooperative pore filling* and *corner flow* events are comparable, and
 370 the invasion front advances in a mixed regime.

371 More generally, the invading front morphology in FIG. 4 can be classified into three
 372 categories: (1) invasion-percolation in strong drainage (mostly “burst” events, $\theta = 160^\circ$),
 373 (2) cooperative pore filling in weak imbibition (mostly “touch” and “overlap” events, $\theta =$
 374 45°), (3) and “post chaining” due to “corner flow” or “capillary bridge” events in strong
 375 imbibition ($\theta = 10^\circ$). The first two categories take place at contact angles between 160° and
 376 45° , and they are very much in line with the quasi-static simulations of Cieplak and Robbins
 377 [23, 24]. The latter category was experimentally observed only recently[27].

378 Furthermore, we find that the finger width measurements (FIG. 12) of the emerging
 379 patterns are in line with experimental observations [15, 16, 27] and numerical predictions
 380 [23, 24]. In strong drainage, the invading patterns have finger width comparable to the size
 381 of a typical pore. When the flow is dominated by cooperative pore filling events, the finger
 382 width diverges to a size of about 18 pores. Finally, the finger width reduces to a fraction of

383 a pore size in corner flow dominated regime. We include the detailed discussion on finger
384 width measurements in Appendix C, and we include video files of the invasion process at
385 different wettabilities in supplementary materials.

386 **Sensitivity of Macroscopic Invasion to Local Contact Angle Perturbations**

387 Any real substrate is bound to have imperfections that perturb local contact angles from
388 the global mean. In the context of the experiments by Zhao *et al.* [27], local imperfections
389 in contact angle could arise from dust deposition on the substrate during fabrication of the
390 microfluidic cell, and one typically takes a great deal of care in minimizing these effects.

391 In practice, no two invasion tests look exactly the same, even when conducted following
392 the same experimental protocol. However, while different realizations of the same experimen-
393 tal conditions can be expected to produce non-identical invasion patterns, those patterns
394 should possess a common quality. This raises an interesting question of quantifying the
395 similarity of the invasion patterns.

396 We mimic local imperfections in contact angle by assigning unique contact angles to
397 every post in the flow geometry. In particular, we select the contact angles from a uniform
398 distribution with 2° range centered around the global mean. FIG. 5 presents the summary
399 from multiple realizations. Every “experiment” was repeated four times for contact angles
400 between 160° and 10° , producing four different realizations for each set of invasion conditions.

401 The degree of similarity of the resulting invasion patterns was assessed by means of two
402 metrics: (1) the percentage of cooperative pore filling events (“touch” and “overlap”), and
403 (2) the fractal dimension of the invasion pattern. The fractal dimension was calculated using
404 the box counting method [38, 39]. The details of the box counting calculations are included
405 in Appendix B.

406 The results in FIG. 5 demonstrate that the percentage of cooperative pore filling events
407 is a robust classifying metric for the invasion shapes; it exhibits negligible variability among
408 realizations. As the contact angle changes from 160° to 45° , “touch” and “overlap” events
409 become dominant. At contact angles below 45° , “corner flow” events take over.

410 In contrast, the fractal dimension shows a higher variability from one realization to an-
411 other, and here we can appreciate the difference in invasion shapes quantitatively. For
412 example, consider the two realizations with $\theta = 84^\circ$ in FIG. 5. At a glance, the two invasion

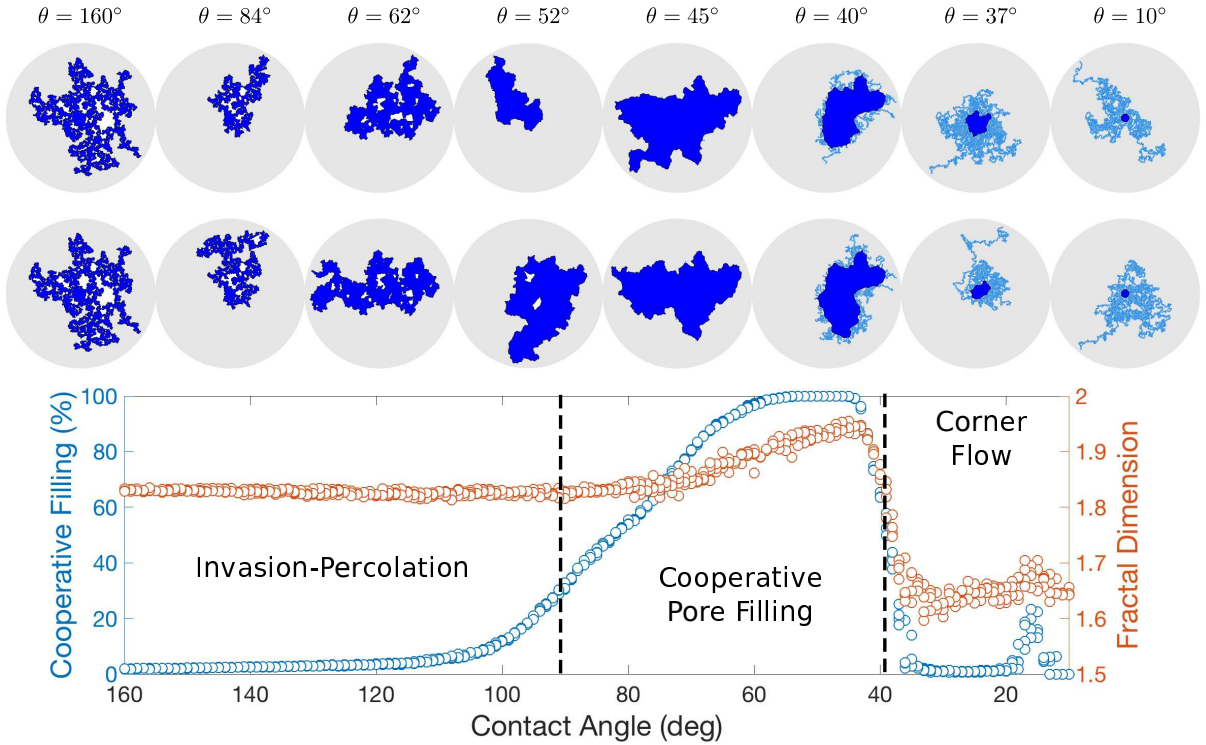


FIG. 5. Cooperative pore filling and fractal dimension plots. Invasion patterns for different realizations at each fixed global contact angle. As the system moves from strong drainage ($\theta = 160^\circ$) to weak imbibition ($\theta = 45^\circ$), the percentage of cooperative pore-filling events gradually increases. The transition from weak to strong imbibition is marked with a sharp drop in both fraction of cooperative pore filling events and fractal dimension.

413 patterns look similar, but there are subtle differences in the invaded regions and clusters of
 414 trapped oil. The fractal dimension reflects this difference, resulting in appreciable scatter of
 415 points at $\theta = 84^\circ$ in FIG. 5.

416 The fractal dimension data reported in FIG. 5 is computed with box counting method,
 417 and shows reasonable values for all flow regimes. The mean fractal dimension for invasion-
 418 percolation is 1.83; for cooperative pore filling is between 1.83 and 1.96; and in the corner
 419 flow regime is 1.65.

420 Overall, we were able to mimic the simulation of the same experimental conditions with lo-
 421 cal imperfections in the wetting properties of the substrate. While every simulation produces
 422 a “unique” pattern, each pattern falls into one of the shape categories (invasion-percolation,
 423 cooperative filling, corner flow) based on the percentage of cooperative pore filling events

424 plot.

425 **Influence of Drainage Overlap and Post Spacing on Cooperative Pore Filling**

426 Consider the schematic diagrams of “drainage overlap” and the original “overlap” events
427 in FIG. 6(a). During the invasion process, the “drainage overlap” always precedes the
428 original “overlap” event of Cieplak and Robbins [23, 24] and thus corresponds to a lower
429 critical pressure. Since we advance the invasion front into pores with lowest critical pressures,
430 by overestimating the critical pressures of “overlap” events, one would erroneously advance
431 the invasion front through spurious “burst” instabilities. This is especially likely to happen
432 when the spacing between the posts is large. We examine the significance of “drainage
433 overlap” by increasing the spacing between posts in the original pore geometry by a factor
434 $\lambda > 1$.

435 FIG. 6(b) shows that by considering “drainage overlap”, we recover a considerable num-
436 ber of cooperative pore filling events otherwise lost if one follows the original definition of
437 “overlap” event of Cieplak and Robbins [23, 24]. Simulations with “drainage overlap” result
438 in about 30% cooperative pore filling event ratio at $\theta = 160^\circ$ for $\lambda = 4$, while the original
439 “overlap” produces no cooperative filling events at $\theta = 160^\circ$ for all λ .

440 One can intuitively understand why larger spacing between posts increases the frequency
441 of cooperative pore filling events by examining two posts and a fluid-fluid interface between
442 them at $\lambda = 1$ and $\lambda = 4$ (FIG. 6(c)). In drainage, as the pressure of the invading fluid
443 increases, the interface approaches its “burst” configuration. When the spacing between the
444 posts is small ($\lambda = 1$), the fluid-fluid interface remains mainly within the gap between the two
445 posts. In contrast, when the spacing is wide ($\lambda = 4$), the interface extrudes significantly away
446 from the gap between two posts before reaching the “burst” configuration. As a result, this
447 interface is more likely to encounter — and coalesce with — the neighboring fluid interfaces.
448 In the extreme limit, when $\lambda \gg 1$, we expect the fluid front to advance mainly through
449 cooperative pore filling via “drainage overlap” events, even in strong drainage. Therefore,
450 the “drainage overlap” presented in section II is crucial for the validity of the quasi-static
451 invasion model on a wide range of pore geometries, especially in simulating multiphase flow
452 through highly porous materials such as low-density micropillar arrays [21] or fibrous media
453 [40–42].

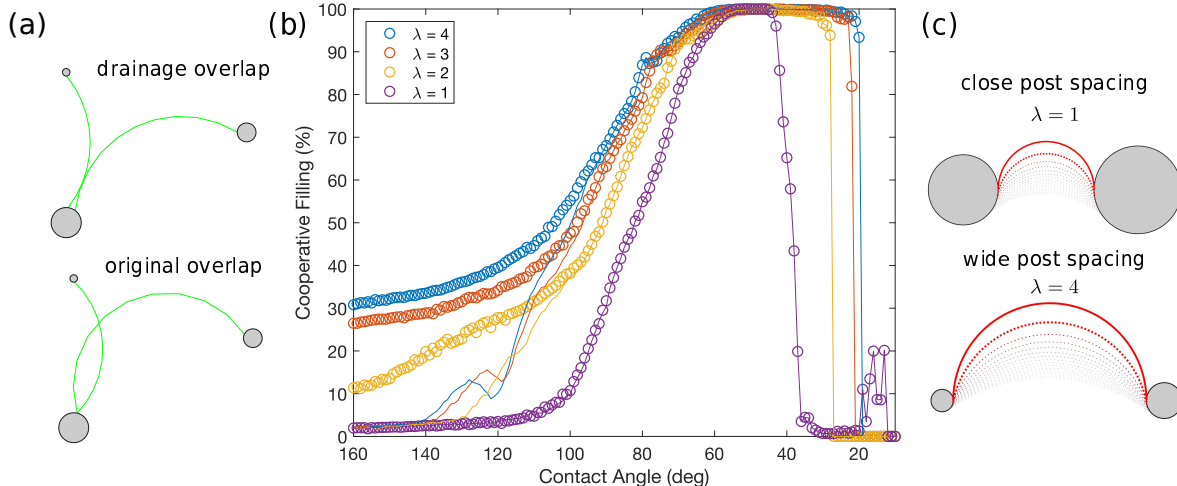


FIG. 6. (a) Schematic diagrams of “drainage overlap” and “overlap” event of Cieplak and Robbins [23, 24]. (b) Percentage of cooperative pore filling events for posts spaced out by a factor of λ from the original post geometry. The colored circles represent simulations with “drainage overlap” considered; solid lines represent simulations with the original “overlap” definition of Cieplak and Robbins [23, 24]. (c) Schematic diagram of post spacing and fluid-fluid interface.

454 The “drainage overlap” events (see section II) result in trapping of the defending liquid on
 455 the surfaces of the posts at $\theta > 90^\circ$ (FIG. 2(b)). Furthermore, the earlier onset of cooperative
 456 pore filling due to λ changes the amount and the manner in which the defending fluid is
 457 trapped behind the invasion front. Trapping of the defending liquid is an interesting problem
 458 on its own, but it is not the focus of this work.

459 Three-Dimensional Effects: Out-of-Plane Curvature

460 In the simulations described so far, we neglected the *out of plane* curvature contributions
 461 in the Young-Laplace equation when calculating critical pressures of “burst”, “touch” and
 462 “overlap” events in section II, akin to the simulations of Cieplak and Robbins [23, 24]. The
 463 ascribed correction to the critical pressures is that $\frac{\Delta p}{\gamma} = \frac{1}{r_p}$ is replaced by $\frac{\Delta p}{\gamma} = \frac{1}{r_p} - \frac{2 \cos \theta}{h}$
 464 for “burst”, “touch”, and “overlap” events.

465 As the height of the posts decreases, the relative magnitudes of the critical pressures
 466 change. This, in turn, alters the final patterns of the invasion fronts (FIG. 7). As the
 467 post heights approach $100\mu m$, the critical pressures of “burst”, “touch”, “overlap” events

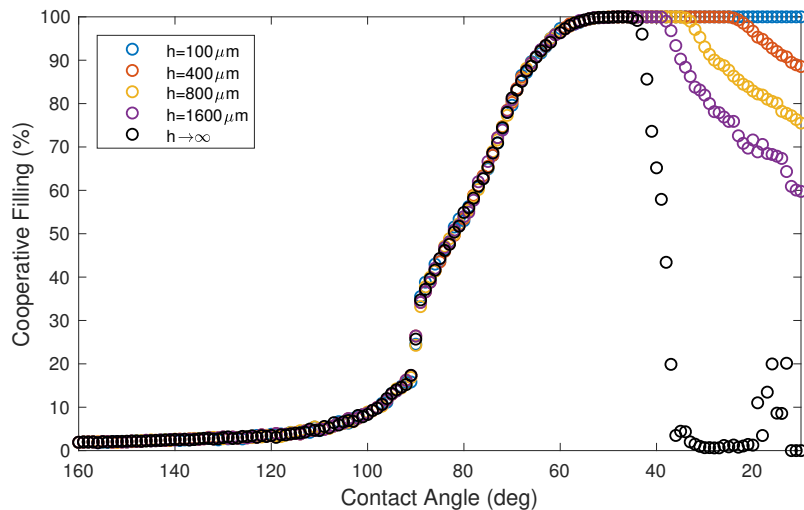


FIG. 7. Figure shows how post heights alter the shapes of the invasion fronts: the onset of the *corner flow* dominated regime is heavily influenced by the out-of-plane curvature correction of the “burst”, “touch”, and “overlap” instabilities. The magnitude of the correction is controlled by the height of the posts. Invasion fronts on the right are plotted for different h at $\theta = 10^\circ$.

468 become lower than critical pressures of “corner” and “capillary bridge” flow events, leading
 469 to a dominance of cooperative pore filling at low contact angles. However, in reality, Zhao
 470 *et al.* [27] observed corner flow dominated regime at $\theta = 7^\circ$.

471 This discrepancy between the experiment and our quasi-static simulations can be due to
 472 several factors. Firstly, this *out of plane* curvature adjustment is rather crude, and was only
 473 implemented to test the limits of our 2D model. A full three-dimensional consideration of the
 474 invasion would be more accurate, although the formulation would also be significantly more
 475 complex. Secondly, and perhaps more importantly, we have likely overestimated the critical
 476 pressures of “corner” events. This can be appreciated from a close examination of invasion
 477 progression at strong imbibition in the experiments of Zhao *et al.* [27]. There, on average,
 478 corner menisci appeared to grow only up to about the middle of pore throats, at which
 479 point the neighbouring posts were coated. In our model, the critical pressures of *corner flow*
 480 events were calculated assuming the full growth of the *corner meniscus* across the throat,
 481 which results in higher critical pressures. Indeed, imposing the *half-throat* rule in our model,
 482 produces a transition to *corner flow* at around $\theta = 22^\circ$. This earlier coating of the posts
 483 could be due to the establishment of a conductive film ahead of the corner meniscus that

484 was not visible in the experimental images. Indeed, the fluid invasion through thin film flow
485 in strong imbibition and accumulation of invading fluid in the corners was also observed by
486 Odier *et al.* [28]. Resolving the detailed dynamics of post bridging in the strong imbibition
487 regime warrants further experimental and theoretical investigations.

488 Furthermore, solid surface roughness in realistic 3D rock geometries may provide conti-
489 nuity to the wetting layers. In the presence of strong surface roughness, growth of the corner
490 menisci would still dominate in strong imbibition, but the morphology of the invading pat-
491 tern would likely be controlled by the heterogeneity in surface roughness rather than the
492 spacing between the posts. While the considerations of roughness and film flow in realistic
493 3D geometries are outside the scope of this work, they are, however, potentially important
494 mechanisms in strong imbibition.

495 IV. CONCLUSIONS

496 Overall, our approach to immiscible fluid invasion in disordered micropillar arrays can be
497 viewed as an extension of the invasion-percolation algorithm to include wettability through
498 critical invasion pressures for cooperative filling and corner flow events. This approach
499 eliminates the need for (and thus the sensitivity to) arbitrary increments in the invading
500 pressures and scanning order of the interface for instability events observed in the earlier
501 work [23, 24]. Our algorithm also allows assigning a unique contact angle to every post, to
502 study the sensitivity of the invasion patterns to local wettability variations.

503 The invasion model presented here was coded into an efficient simulation algorithm,
504 making it an attractive starting point for dynamic pore invasion simulations. A natural
505 way of extending this algorithm is through incorporating viscous forces with a coupled pore-
506 network model [31, 43, 44].

507 We have tested the invasion model by comparing the simulation outputs with the ex-
508 periments of Zhao *et al.* [27]. Our quasi-static model was able to capture the nature of
509 the invasion fronts at low capillary numbers for the full range of substrate wettabilities,
510 including the transition from *invasion-percolation* to *cooperative filling* to *corner flow* as a
511 function of contact angle. This can have important implications in enhanced oil recovery,
512 carbon sequestration, and microfluidic applications. For example, in petroleum production,
513 a more compact invasion pattern is preferred when displacing oil from the reservoir by water

514 injection. In some instances of reactive transport in microfluidic applications, however, one
515 might want to induce the fingering invasion to maximize the interface area between invading
516 and defending liquids.

517 Fluid injection can result in localized redistribution of stress loads within porous media
518 accompanied with dilation of the pore space [43, 44]. Some of the recent experimental obser-
519 vations of pore-scale poroelasticity include localized fluid-induced deformation of hydrogel
520 packs[45] and glass bead pack deformation caused by immiscible liquid infiltration[46–48].
521 The dynamic extension of the model presented here could be further extended to include
522 pore deformations due to changes in effective stress under different wettability conditions,
523 which could capture the potential interplay between pore wettability and deformation during
524 fluid-fluid displacement.

525 **V. ACKNOWLEDGEMENTS**

526 We would like to thank Amir Pahlavan for insightful discussions. This work was partly
527 funded by the US Department of Energy (grant DE-SC0018357).

528 **Appendix A: Corner Meniscus**

529 In this appendix we examine the shape of the corner meniscus around a typical post. We
530 follow a similar derivation to that of the droplet shape on a fiber [37]. We treat our post
531 as a fiber and impose desired contact angles as boundary conditions at the interface ends,
532 imposing that contact angles of θ are maintained at both post and plate contacts. Finally,
533 we examine the growth and potential mid-post coalescence of the top/bottom menisci.

534 **1. Corner Meniscus Shape**

535 Here we determine how far the meniscus extends in the horizontal and vertical directions
536 for a given Laplace pressure, and check whether the force balance equation suggested in this
537 work adequately captures the horizontal extent of the meniscus.

538 FIG. 8 shows a cross section of the corner meniscus around a post with radius r_1 . By
539 developing an argument very similar to the formulation of the droplet shape on a fiber of

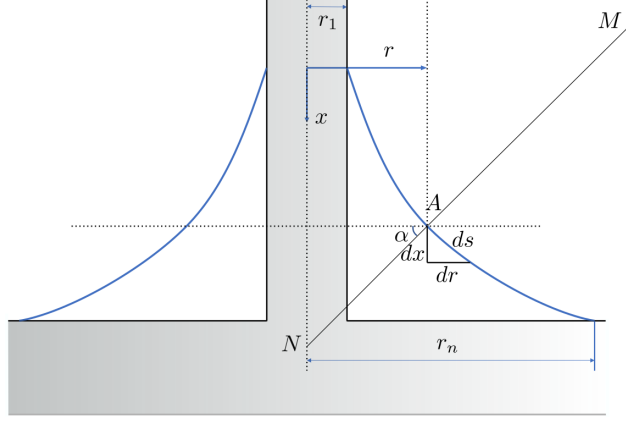


FIG. 8. Shape of the corner meniscus around the post with radius r_1 . AM and AN are the principal radii of curvature at point A, where AM is in plane and AN is perpendicular to the plane.

540 De Gennes *et al.* [37], we can find the meniscus shape equation. We start with the Young-
 541 Laplace equation for an arbitrary point A on the liquid interface:

$$542 \quad \frac{1}{AN} - \frac{1}{AM} = \frac{\Delta p}{\gamma}. \quad (\text{A1})$$

543 Noting that $r = AN \cdot \cos \alpha$ and $ds = AM \cdot d\alpha$, Equation (A1) can be written as:

$$544 \quad \frac{\cos \alpha}{r} - \frac{d\alpha}{ds} = \frac{\cos \alpha}{r} - \frac{d\alpha}{dr} \frac{dr}{ds} = \frac{\Delta p}{\gamma}. \quad (\text{A2})$$

545 Furthermore, $dr = \sin \alpha ds$, so the Young-Laplace equation takes the following form:

$$546 \quad \frac{\cos \alpha}{r} - \frac{d\alpha}{dr} \sin \alpha = \frac{\Delta p}{\gamma}. \quad (\text{A3})$$

547 Noting that $dr = \sin \alpha ds$ and $dx = \cos \alpha ds$,

$$548 \quad \frac{dx}{dr} = \dot{x} = \cot \alpha. \quad (\text{A4})$$

549 Squaring both sides of Equation (A4) leads to the following equations:

$$550 \quad \sin \alpha = \frac{1}{(1 + \dot{x}^2)^{1/2}}, \quad (\text{A5a})$$

$$551 \quad \cos \alpha = \frac{\dot{x}}{(1 + \dot{x}^2)^{1/2}}. \quad (\text{A5b})$$

552 Differentiating Equation (A4) with respect to r , yields:

$$553 \quad \ddot{x} = -\frac{1}{\sin^2 \alpha} \frac{d\alpha}{dr}. \quad (\text{A6})$$

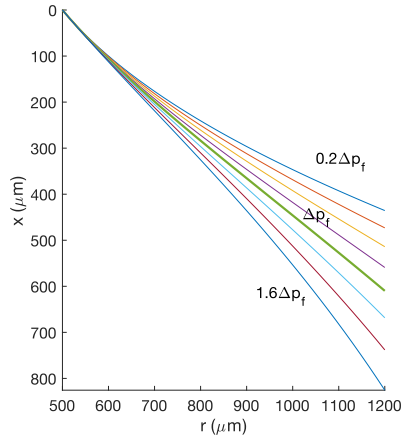


FIG. 9. Interface shape of a corner meniscus outside a post. Equation (A7) solved with $\theta = 40^\circ$, $r_1 = 500\mu m$, $r_n = 1200\mu m$. Here, Δp_f represents the Laplace pressure obtained from the force balance Equation (7). Condition $\dot{x}(r_n) = \tan \theta_1$ is exactly satisfied when $\Delta p = \Delta p_f$.

554 Finally, substituting Equations (A5) and (A6) into Equation (A3), we obtain the final
 555 equation for the liquid interface:

$$556 \quad \frac{\dot{x}}{r(1 + \dot{x}^2)^{1/2}} + \frac{\ddot{x}}{(1 + \dot{x}^2)^{3/2}} = \frac{\Delta p}{\gamma}. \quad (\text{A7})$$

557 Now, Equation (A7) with $\dot{x}(r_1) = \cot \theta_1$ and $x(r_1) = 0$ can be used to find the corner
 558 meniscus profile. FIG. 9 shows the solution of Equation (A7) for $r = (r_1, r_n)$ with a typical
 559 geometry and contact angle used in this study.

560 The pressure drop across the interface should be such that $\dot{x}(r_n) = \tan \theta_1$. It turns out
 561 that this condition is exactly satisfied when Δp is calculated from the force balance equation
 562 (7). This verifies the validity of the force balance approach in finding critical values of Δp
 563 for *corner flow*.

564 At the same time, FIG. 9 shows that the extent of the corner meniscus is of comparable
 565 size in horizontal and vertical directions. Since the height of the posts in Zhao *et al.* [27]
 566 experiments is $100\mu m$, we need to consider two cases: (1) corner menisci at the top and
 567 bottom which do not touch; and (2) corner menisci that meet and merge at the mid-height
 568 of the cell. When the liquid menisci do not meet in the middle of the post, the critical Δp
 569 for *corner flow* can be estimated from the force balance equation (7). However, when corner
 570 liquids meet, the shape of the interface can be estimated as a *capillary bridge* between two
 571 flat plates, described by the equation [37]:

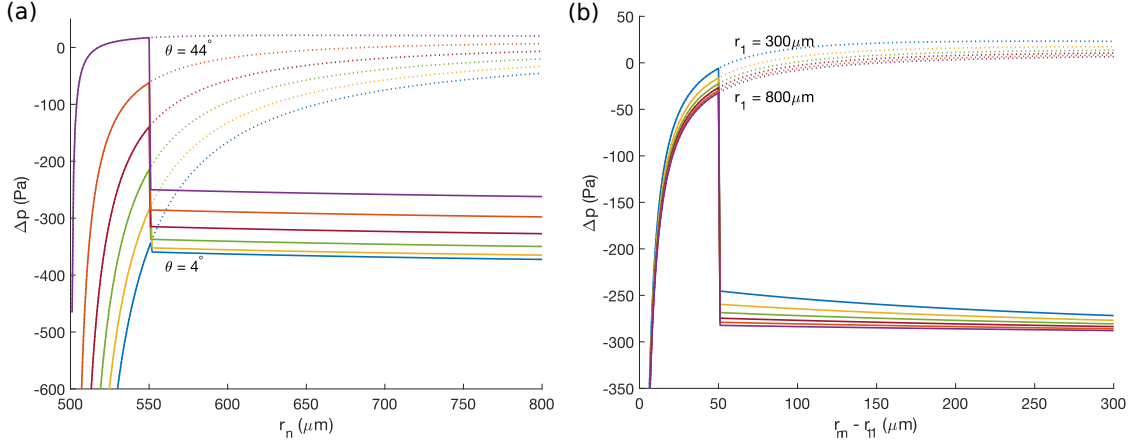


FIG. 10. Laplace pressure for a growing corner meniscus. Initially, the invading liquid is confined to the corners. As the horizontal extent of the liquid grows, the top and bottom corners meet at the mid-height of the post, and the shape changes into a capillary bridge. This transition point corresponds to the negative jump in Laplace pressure. (a) Evolution of the corner menisci for contact angles between 4° and 44° and $r_1 = 500 \mu\text{m}$. (b) Evolution of the corner menisci for post radii between $300 \mu\text{m}$ and $800 \mu\text{m}$ and contact angle of 40° .

572

$$\frac{1}{r_n - \frac{h}{2 \cos \theta_1} (1 - \sin \theta_1)} - \frac{2 \cos \theta_1}{h} = \frac{\Delta p}{\gamma} \quad (\text{A8})$$

573

2. Corner Meniscus Growth

574

575

576

577

578

579

580

581

582

583

584

We now consider the growth of the corner meniscus on a post with height of $100 \mu\text{m}$ (FIG. 10(a)). At first, the invading liquid is confined to the top and bottom corners of the post—growth of the meniscus in the horizontal direction increases the Laplace pressure requirement. Top and bottom menisci grow to the point that they touch at mid-height of the post. At this point, the shape of the corner liquid changes into a capillary bridge.

We make the following observations. Firstly, before the menisci merge, the Laplace pressure increases with growing r_n . After they merge, the shape turns into a capillary bridge, and the Laplace pressure decreases with growing r_n . This means that if the liquid invasion was stimulated with small pressure increments, the corner liquid would grow gradually with increasing Δp , and then grow spontaneously after assuming a capillary bridge shape.

Secondly, the magnitude of the discontinuity in Δp at the corner liquid *merger* point is

585 smaller at low contact angles (FIG. 10(a)). This can be explained intuitively by visualizing
 586 the corner merging instant at contact angles of 0° and 45° . For $\theta = 0^\circ$, when two corner
 587 liquids meet at the mid-height of the post, $\frac{dr}{dx}|_{x=h/2} = 0$ both before and after the merger.
 588 However, for $\theta = 45^\circ$, $\frac{dr}{dx}|_{x=h/2} = 1$ before and $\frac{dr}{dx}|_{x=h/2} = 0$ after the merger. This means that
 589 at 45° the invading liquid needs to “snap” from the *corner* to *bridge* shape. The magnitude
 590 of this “snap” is small at contact angles near 0° .

591 Finally, FIG. 10(b) shows that the Laplace pressure is smaller for larger posts. The out-
 592 of-plane radius of curvature (AN in FIG. 8) is always greater than the radius of the post,
 593 and hence posts with greater radius correspond to lower Laplace pressures (Equation (A1)).
 594 In other words, it is easier to grow the corner menisci around the posts with larger radius.

595 Appendix B: Measuring Fractal Dimension

596 The morphology of the invading fluid phase can be complex (FIG. 4), and fractal dimen-
 597 sion can be an intuitive way to capture this complexity. Fractal dimension can be thought
 598 of as an “index of the scale-dependency of a pattern” [38]. In this work, we utilize the box-
 599 counting method [38, 39] to estimate the fractal dimension of the invading fluid patterns.

600 The box counting method iteratively tiles the image containing the flow pattern with
 601 boxes of size ϵ . Each iteration uses increasingly greater value of ϵ and measures the number
 602 N of boxes that contain (or “directly cover”) the flow pattern. The magnitude of the slope
 603 of N against ϵ on a log-log plot defines the box-counting fractal dimension [39].

604 To estimate the fractal dimension of the invading fluid we took the following steps: (1)
 605 obtain the invasion pattern image from the simulation, with fully surrounded posts treated
 606 as part of the invading phase (FIG. 11(a)); this step typically produced images of 1200×1200
 607 pixels in size; (2) convert image to black and white (FIG. 11(b)); (3) grid the image with
 608 boxes of size ϵ between 1 and the number of pixels in each direction of the image (n_{pix})
 609 (FIG. 11(c)-(d)); (4) record the number N of boxes required to fill the pattern for each ϵ ;
 610 (5) calculate the fractal dimension as an absolute value of the slope of N against ϵ on a
 611 log-log plot (FIG. 11(e)).

612 When calculating the slope of N against ϵ on the log-log plot, we imposed user-defined
 613 expectations on the bounds of the fractal behavior. We exclude the boxes close to the image
 614 size, so we set $\epsilon < \frac{n_{\text{pix}}}{8}$.

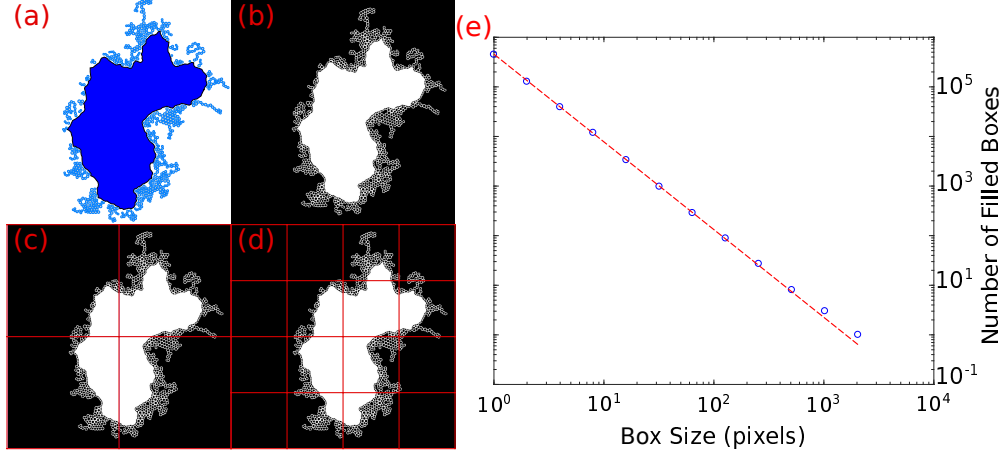


FIG. 11. Fractal dimensions calculated with the box-counting method. (a) color image (1500×1500 pixels) produced by the invasion algorithm for $\theta = 40^\circ$; (b)-(d) black and white versions of the invasion pattern placed on a grid of size $\epsilon = [1, n_{\text{pix}}]$; (e) fractal dimension measured as a slope of number N of filled boxes against ϵ on a log-log plot, slope was calculated from points with $\epsilon = [1, \frac{n_{\text{pix}}}{8}]$.

Appendix C: Measuring Finger Width

In order to estimate the invading fluid finger width (w), Cieplak and Robbins [23, 24] put forward the following method. First, they slice the invasion pattern along the nodes of their regular lattice. Then, they measure the size of the invaded region clusters along each 1D slice. The mean size of the clusters was taken as an estimate of w , which was then divided by the lattice length a .

We cannot follow the method of Cieplak and Robbins [23, 24] precisely since our post geometry was built on an irregular lattice. We use a close equivalent estimate of w instead. We start with black and white images used to measure box-counting fractal dimension and slice it into separate rows. We collect the statistic of the invading clusters in resulting slices using MATLAB's `bwconncomp` function, where mean size of the clusters estimates w in pixels. We repeat the same procedure on an image where pore spaces and posts have white and black colors respectively. This allows estimating a as an average pore size in pixels. Thus, we recover the w/a used by Cieplak and Robbins. The above procedure was repeated for vertical slices as well.

FIG. 12 shows that the finger width spans several pores in the invasion-percolation regime,

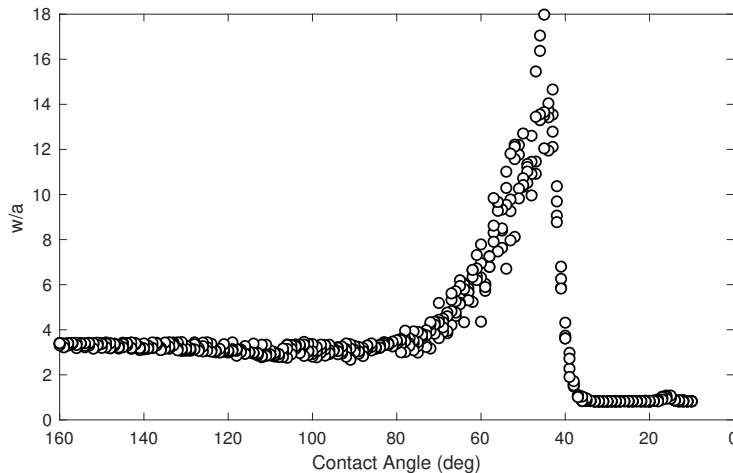


FIG. 12. Ratio of the invading pattern finger width to mean pore size, estimated in analogy to the work of Cieplak and Robbins [23, 24].

631 and starts diverging at contact angles below 60° . This growth of finger width is abruptly
 632 interrupted below 40° , where fluid invasion is dominated by corner flow and w is only a
 633 fraction of the mean pore size a .

-
- 634 [1] Jing-Den Chen and David Wilkinson, “Pore-scale viscous fingering in porous media,” *Physical*
 635 *Review Letters* **55**, 1892–1895 (1985).
- 636 [2] Knut Jørgen Måløy, Jens Feder, and Torstein Jøssang, “Viscous fingering fractals in porous
 637 media,” *Physical Review Letters* **55**, 2688 (1985).
- 638 [3] Lincoln Paterson, “Diffusion-limited aggregation and two-fluid displacements in porous me-
 639 dia,” *Physical Review Letters* **52**, 1621 (1984).
- 640 [4] L Niemeyer, Luciano Pietronero, and HJ Wiesmann, “Fractal dimension of dielectric break-
 641 down,” *Physical Review Letters* **52**, 1033 (1984).
- 642 [5] P Meakin, Susan Tolman, and A Blumen, “Diffusion-limited aggregation,” *Proceedings of*
 643 *the Royal Society of London A: Mathematical and Physical Sciences* **423**, 133–148 (1989).
- 644 [6] Massimo Conti and Umberto Marini Bettolo Marconi, “Diffusion limited propagation of burn-
 645 ing fronts,” *WIT Transactions on Ecology and the Environment* **137**, 37–45 (2010).
- 646 [7] S. Hill, “Channeling in packed columns,” *Chemical Engineering Science* **1**, 247–253 (1952).

- 647 [8] Ryan Anderson, Lifeng Zhang, Yulong Ding, Mauricio Blanco, Xiaotao Bi, and David P
648 Wilkinson, “A critical review of two-phase flow in gas flow channels of proton exchange mem-
649 brane fuel cells,” *Journal of Power Sources* **195**, 4531–4553 (2010).
- 650 [9] Yildiray Cinar, Amir Riaz, and Hamdi A Tchelepi, “Experimental study of CO₂ injection
651 into saline formations,” *SPE Journal* **14**, 588–594 (2009).
- 652 [10] Larry W Lake, *Enhanced oil recovery* (Prentice-Hall, Englewood Cliffs, NJ, 1989).
- 653 [11] Hyundo Lee, Ankur Gupta, T Alan Hatton, and Patrick S Doyle, “Creating isolated liquid
654 compartments using photopatterned obstacles in microfluidics,” *Physical Review Applied* **7**,
655 044013 (2017).
- 656 [12] Richard L Hoffman, “A study of the advancing interface,” *Journal of Colloid and Interface
657 Science* **50**, 228–241 (1975).
- 658 [13] Bertrand Levaché and Denis Bartolo, “Revisiting the saffman-taylor experiment: Imbibition
659 patterns and liquid-entrainment transitions,” *Physical Review Letters* **113**, 044501 (2014).
- 660 [14] Benzhong Zhao, Amir Alizadeh Pahlavan, Luis Cueto-Felgueroso, and Ruben Juanes, “Forced
661 wetting transition and bubble pinch-off in a capillary tube,” *Physical Review Letters* **120**,
662 084501 (2018).
- 663 [15] JP Stokes, DA Weitz, Jerry P Gollub, A Dougherty, MO Robbins, PM Chaikin, and HM Lind-
664 say, “Interfacial stability of immiscible displacement in a porous medium,” *Physical Review
665 Letters* **57**, 1718 (1986).
- 666 [16] Mathias Trojer, Michael L Szulczewski, and Ruben Juanes, “Stabilizing fluid-fluid displace-
667 ments in porous media through wettability alteration,” *Physical Review Applied* **3**, 054008
668 (2015).
- 669 [17] Roland Lenormand, Cesar Zarcone, and A Sarr, “Mechanisms of the displacement of one fluid
670 by another in a network of capillary ducts,” *Journal of Fluid Mechanics* **135**, 337–353 (1983).
- 671 [18] Roland Lenormand and Cesar Zarcone, “Invasion percolation in an etched network: Measure-
672 ment of a fractal dimension,” *Physical Review Letters* **54**, 2226–2229 (1985).
- 673 [19] Roland Lenormand, Eric Touboul, and Cesar Zarcone, “Numerical models and experiments on
674 immiscible displacements in porous media,” *Journal of Fluid Mechanics* **189**, 165–187 (1988).
- 675 [20] Richard Chandler, Joel Koplik, Kenneth Lerman, and Jorge F Willemsen, “Capillary displace-
676 ment and percolation in porous media,” *Journal of Fluid Mechanics* **119**, 249–267 (1982).
- 677 [21] Michael Jung, Martin Brinkmann, Ralf Seemann, Thomas Hiller, Marta Sanchez de La Lama,

- 678 and Stephan Herminghaus, “Wettability controls slow immiscible displacement through local
679 interfacial instabilities,” *Physical Review Fluids* **1**, 074202 (2016).
- 680 [22] Kamaljit Singh, Hagen Scholl, Martin Brinkmann, Marco Di Michiel, Mario Scheel, Stephan
681 Herminghaus, and Ralf Seemann, “The role of local instabilities in fluid invasion into perme-
682 able media,” *Scientific Reports* **7**, 444 (2017).
- 683 [23] Marek Cieplak and Mark O Robbins, “Dynamical transition in quasistatic fluid invasion in
684 porous media,” *Physical Review Letters* **60**, 2042–2045 (1988).
- 685 [24] Marek Cieplak and Mark O. Robbins, “Influence of contact angle on quasistatic fluid invasion
686 of porous media,” *Physical Review B* **41**, 11508–11521 (1990).
- 687 [25] P. G. Saffman and G Taylor, “The penetration of a fluid into a porous medium or Hele-
688 Shaw cell containing a more viscous liquid,” *Proceedings of the Royal Society of London A:
689 Mathematical, Physical and Engineering Sciences* **245**, 312–329 (1958).
- 690 [26] R L Chuoke, P van Meurs, and C. van der Poel, “The instability of slow, immiscible, viscous
691 liquid-liquid displacements in permeable media,” *Petroleum Transactions, AIME* **216**, 188–194
692 (1959).
- 693 [27] Benzhong Zhao, Christopher W MacMinn, and Ruben Juanes, “Wettability control on mul-
694 tiphase flow in patterned microfluidics,” *Proceedings of the National Academy of Sciences of
695 the USA* **113**, 10251–10256 (2016).
- 696 [28] Céleste Odier, Bertrand Levaché, Enrich Santanach-Carreras, and Denis Bartolo, “Forced
697 imbibition in porous media: A fourfold scenario,” *Physical Review Letters* **119**, 208005 (2017).
- 698 [29] Paul Meakin and Alexandre M Tartakovsky, “Modeling and simulation of pore-scale multi-
699 phase fluid flow and reactive transport in fractured and porous media,” *Reviews of Geophysics*
700 **47**, RG3002 (2009).
- 701 [30] Martin J Blunt, “Flow in porous media—pore-network models and multiphase flow,” *Current
702 Opinion in Colloid and Interface Science* **6**, 197–207 (2001).
- 703 [31] Ran Holtzman and Enrico Segre, “Wettability stabilizes fluid invasion into porous media via
704 nonlocal, cooperative pore filling,” *Physical Review Letters* **115**, 164501 (2015).
- 705 [32] Ran Holtzman, “Effects of pore-scale disorder on fluid displacement in partially-wettable
706 porous media,” *Scientific Reports* **6**, 36221 (2016).
- 707 [33] Martin J Blunt, “Physically-based network modeling of multiphase flow in intermediate-wet
708 porous media,” *Journal of Petroleum Science and Engineering* **20**, 117–125 (1998).

- 709 [34] Mohammed S Al-Gharbi and Martin J Blunt, “Dynamic network modeling of two-phase
710 drainage in porous media,” *Physical Review E* **71**, 016308 (2005).
- 711 [35] R Lenormand and S Bories, “Description d’un mecanisme de connexion de liaison destine
712 a l’etude du drainage avec piegeage en milieu poreux,” *Comptes Rendus de l’Académie des*
713 *Sciences* **291**, 279–282 (1980).
- 714 [36] David Wilkinson and Jorge F Willemsen, “Invasion percolation: a new form of percolation
715 theory,” *Journal of Physics A: Mathematical and General* **16**, 3365–3376 (1983).
- 716 [37] Pierre-Gilles De Gennes, Françoise Brochard-Wyart, and David Quéré, *Capillarity and Wet-*
717 *ting Phenomena: Drops, Bubbles, Pearls, Waves* (Springer Science & Business Media, 2013).
- 718 [38] NC Kenkel and DJ Walker, “Fractals in the biological sciences,” *Coenoses* **11**, 77–100 (1996).
- 719 [39] Philip M Iannaccone and Mustafa Khokha, *Fractal Geometry in Biological Systems: an Ana-*
720 *lytical Approach* (CRC Press, 1996).
- 721 [40] RL Peek Jr and DA McLean, “Capillary penetration of fibrous materials,” *Industrial & En-*
722 *gineering Chemistry Analytical Edition* **6**, 85–90 (1934).
- 723 [41] Karsten E Thompson, “Pore-scale modeling of fluid transport in disordered fibrous materials,”
724 *AIChE journal* **48**, 1369–1389 (2002).
- 725 [42] RB Calhoun and A Mortensen, “Infiltration of fibrous preforms by a pure metal,” *Metallurgical*
726 *Transactions A* **23**, 2291–2299 (1992).
- 727 [43] AK Jain and R Juanes, “Preferential mode of gas invasion in sediments: Grain-scale mecha-
728 nistic model of coupled multiphase fluid flow and sediment mechanics,” *Journal of Geophysical*
729 *Research: Solid Earth* **114**, B08101 (2009).
- 730 [44] Ran Holtzman and Ruben Juanes, “Crossover from fingering to fracturing in deformable
731 disordered media,” *Physical Review E* **82**, 046305 (2010).
- 732 [45] Christopher W MacMinn, Eric R Dufresne, and John S Wettlaufer, “Fluid-driven deformation
733 of a soft granular material,” *Physical Review X* **5**, 011020 (2015).
- 734 [46] M. J. Dalbe and R. Juanes, “Morphodynamics of fluid-fluid displacement in 3D deformable
735 granular media.” *Physical Review Applied* **9**, 024028 (2018).
- 736 [47] Ran Holtzman, Michael L Szulczewski, and Ruben Juanes, “Capillary fracturing in granular
737 media,” *Physical Review Letters* **108**, 264504 (2012).
- 738 [48] M. Trojer, P. de Anna, and R. Juanes, “Impact of wetting on fracturing of granular media.”
739 Submitted.